Combining Inertial Measurements With Blind Image Deblurring Using Distance Transform

Yi Zhang, *Member, IEEE*, and Keigo Hirakawa, *Senior Member, IEEE*

Abstract—Camera motion during exposure leads to a blurry image. We propose an image deblurring method that infers the blur kernel by combining the inertial measurement unit (IMU) data that track camera motion with techniques that seek blur cues from the image sensor data. Specifically, we introduce the notion of IMU fidelity cost designed to penalize blur kernels that are unlikely to have yielded the observed IMU measurements. When combined with the image data-based fidelity and regularization terms used by the conventional blind image deblurring techniques, the overall energy function is nonconvex. We solved this nonconvex energy minimization problem by a novel use of distance transform, recovering a blur kernel and sharp image that are consistent with the IMU and image sensor measurements.

Index Terms—Blind image deblurring, blur kernel estimation, convex optimization, distance transform, homography, IMU fidelity, sensor fusion, spatially varying blur.

I. INTRODUCTION

IMAGE blur is a phenomenon caused by the pixel sensors recording light originating from multiple points in the scene. Blur arisen from camera motion is a chronic problem in low light photography—i.e. camera sensor accumulates more photons by increasing exposure time to overcome noise at the risk of camera shake. Such motion blur is typically spatially gradually varying, though it is sometimes approximated by a spatially invariant point spread function (or PSF) for computational simplicity. Despite such simplification, image deblurring is still considered ill-conditioned because both the sharp image and the PSF are unknown.

Blind image deblurring refers to the problem of recovering the latent blur kernel and the sharp image from the observed blurry image alone. Conventionally, it is solved by minimizing an energy function or maximizing posterior density with sparsity constraints over the statistics of latent sharp image and blur kernel [1]–[9]. This is a highly ill-posed problem, however, and so the stability of the existing methods varies greatly. We also argue that blind image deblurring techniques are underutilizing hardware, at least in the sense that inertial sensors such as gyroscope and accelerometer that are already equipped in

contemporary consumer imaging devices [10] are ignored by these algorithms. Measurements from such type of sensors provide blur kernel information that should improve image deblurring.

First proposed by Barnard *et al.* [11] and later extended by many [12]–[14], the existing work use gyroscopes and accelerometers in an inertial measurement unit (IMU) to reconstruct the blur kernel, simplifying the image deblurring problem to a non-blind one with a "known" blur kernel. Joshi *et al.* [12] estimate the camera motion from a camera hot shoe triggered-IMU with 6 degree-of-freedom (DOF) by correcting erroneous accelerometer data using energy minimization. Bae *et al.* [13] used a depth sensor to better estimate the spatially varying blur induced by acceleration. Šindelář and Šroubek [14] developed a real-time deblurring on mobile devices based on a spatially invariant blur approximation. Ringaby and Forssén [15], Park and Levoy [16], and Jia and Evans [17] further investigate the compensation for the sensor bias and the time delay by utilizing multiple frames. Yet, the combination of IMU-based blur kernel estimation and non-blind image deblurring does not yield state-of-the-art results because IMU measurements suffer from noise, bias or drift, sensitivity to gravity, and poor synchronization with the image sensor [see Fig. 2(b)]. Notice also that at the blur kernel estimation stage, methods in [11]–[14] are decoupled from image sensor data, despite the fact that blurred image itself provides rich evidence of the blur kernel.

The goal of this article is to remove the camera shake from a single image efficiently, with the help of an additional IMU sensor (Fig. 1). We propose to modify the standard blind image deblurring framework by introducing an "IMU fidelity" term, aimed at quantifying the similarity between the recovered blur and the raw IMU measurements. By doing so, we estimate blur kernel and sharp image that are consistent with the observed blurry image and the IMU measurements. For example, the drift and the noise of IMU can be corrected with the help of an image sensor data, while the IMU measurements help to overcome the ill-posedness of blind deblurring techniques by constraining a set of feasible solutions. The main challenge associated with the proposed IMU fidelity term is the non-linear relationship between the IMU measurements and the implied blur kernel. This makes the overall energy function highly non-convex, which cannot be solved by the conventional means. A major contribution of our work is a novel technique for solving this difficult energy minimization problem using a distance transform.

The proposed IMU fidelity term and its distance transform solution can be combined with most state-of-the-art blind image deblurring work. We demonstrate the effectiveness of our approach by modifying the spatially invariant blind image
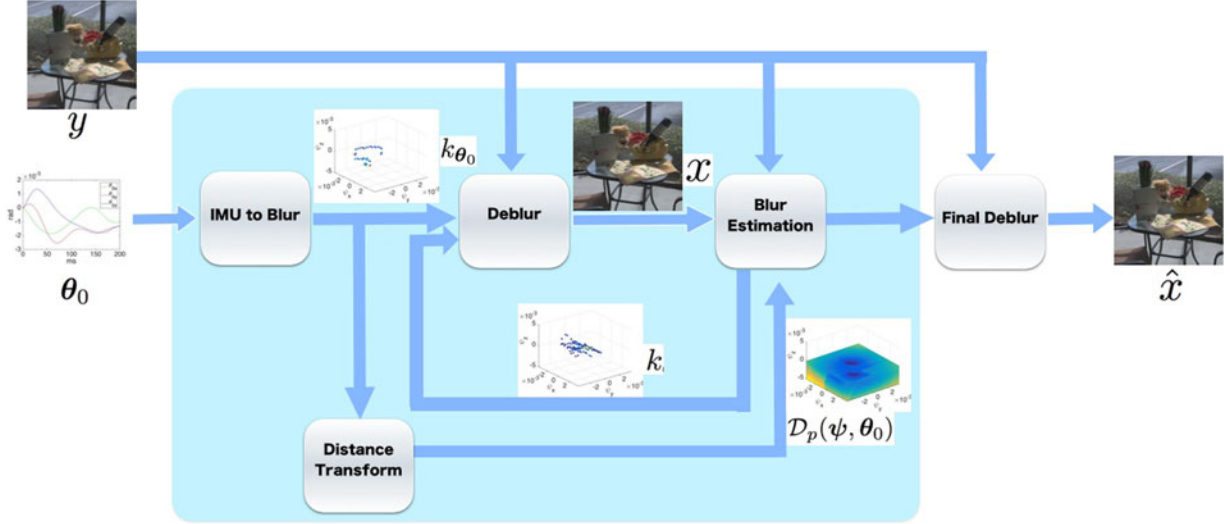
Fig. 1. Illustration of the proposed deblurring pipeline. The IMU measurement is incorporated in each iteration.
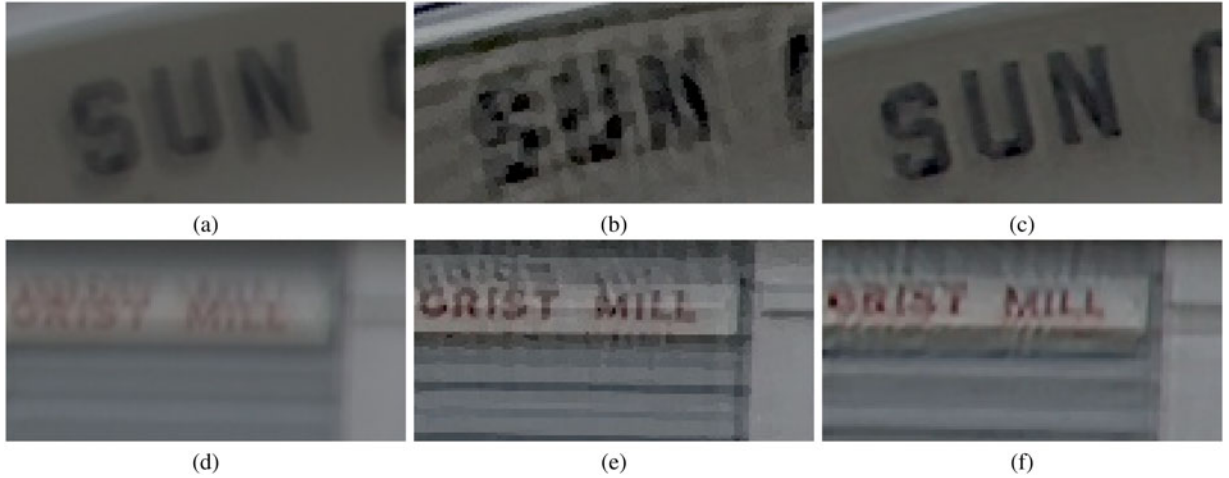

Fig. 2. Examples illustrating the limitation of the existing methods. (a, d) Input images. (b, e) Non-blind deblurring using [19] with the blur kernel reconstructed from the raw IMU data. (c, f) Image-based blind deblurring in [6] that ignores the IMU. Though all deblurred images are unsatisfactory, blind deblurring is more successful than the IMU ones in (b) and (c), while in (e) and (f) the opposite is true.

deblurring methods of [6], [18], as well as the spatially vary-ing blind image deblurring method of [9]. We also prove theo-retically and verify experimentally that our approach tolerates moderate levels of synchronization errors.

II. RELATED WORK

A. Background in IMU-Based Image Deblurring

Camera shake blur is caused by the integration of (unknown) camera motions during the exposure. Motion can be mod-eled by a 3-axis translation $\boldsymbol{\rho} = [\rho_x, \rho_y, \rho_z]^T$ and a rotation $\boldsymbol{\psi} = [\psi_x, \psi_y, \psi_z]^T$ as illustrated in Fig. 3(a). Let the camera intrinsic matrix be denoted by

$$\mathcal{K} = \begin{bmatrix} f & \gamma & c_{x0} \\ 0 & f & c_{y0} \\ 0 & 0 & 1 \end{bmatrix}, \tag{1}$$

where f is the focal length, c_{x0}, c_{y0} are the principal point, and γ is the skew parameter (set to 0 when the image sensor pixels are square). The parameters of intrinsic matrix can be obtained via calibration [20]. Assuming a constant scene depth d, and letting $\boldsymbol{N}$ denote the normal vector of the scene, the real world scene and its 2D projection on the camera sensor plane is related by a homography transform [21]:

$$\mathcal{H}(\boldsymbol{\rho}, \boldsymbol{\psi}) = \mathcal{K} \left\{ R(\boldsymbol{\psi}) + \frac{\boldsymbol{\rho} \boldsymbol{N}^T}{d} \right\} \mathcal{K}^{-1}, \tag{2}$$

where

$$R(\boldsymbol{\psi}) = \begin{bmatrix} \cos \psi_x & -\sin \psi_x & 0 \\ \sin \psi_x & \cos \psi_x & 0 \\ 0 & 0 & 1 \end{bmatrix} \times \begin{bmatrix} \cos \psi_y & 0 & \sin \psi_y \\ 0 & 1 & 0 \\ -\sin \psi_y & 0 & \cos \psi_y \end{bmatrix}$$

$$\times \begin{bmatrix} 1 & 0 & 0 \\ 0 & \cos \psi_z & -\sin \psi_z \\ 0 & \sin \psi_z & \cos \psi_z \end{bmatrix}, \tag{3}$$
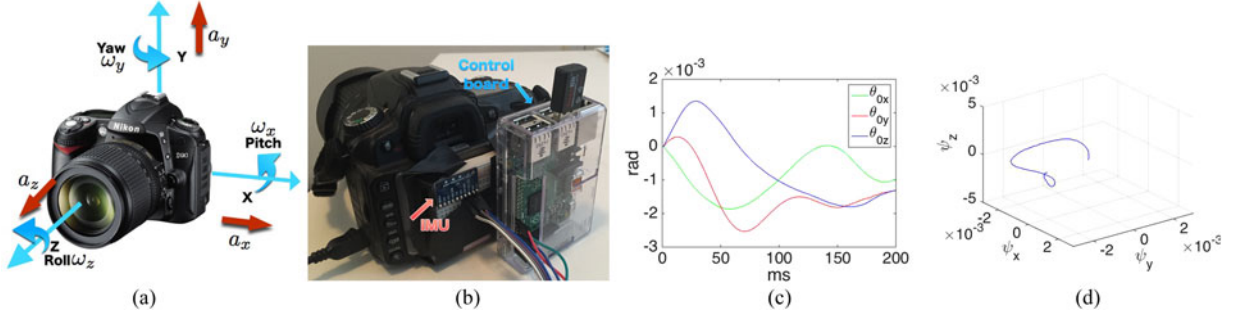
Fig. 3. Illustration of the camera inertial measurements and the corresponding blur kernel. (a) 3-axis acceleration and 3-axis rotation model the camera motion. (b) Customized camera system records the camera inertia during the exposure. (c) Camera rotation $\boldsymbol{\theta}_0$ is the temporal accumulation of the angular speed measured by the gyroscope, and (d) the effective blur kernel $k_{\boldsymbol{\theta}_0}(\boldsymbol{\psi})$ obtained using (7).

denotes the rotation matrix. The image observed by the camera is $x(\mathcal{H}(\boldsymbol{\rho}, \boldsymbol{\psi})\boldsymbol{n})$, where $\boldsymbol{n} \in \mathbb{R}^2$ denotes a two dimensional spatial location and $x : \mathbb{R}^2 \to \mathbb{R}$ is the image at $\boldsymbol{\psi} = \boldsymbol{\rho} = 0$. In practice, the rotation $\boldsymbol{\psi}$ has major effect to the image blur and the translation $\boldsymbol{\rho}$ can be neglected when the scene is sufficiently far away [6], [9], [14]. Under this scenario, (2) simplifies to:

$$\mathcal{H}(\boldsymbol{\psi}) = \mathcal{K}R(\boldsymbol{\psi})\mathcal{K}^{-1}. \tag{4}$$

Camera shake blur is caused by the fact that the rotation and the translation do not remain constant over the exposure time. Let $\boldsymbol{\theta}(t) = [\theta_x(t), \theta_y(t), \theta_z(t)]$ denote the camera rotation $\boldsymbol{\psi}$ at time t. Assuming a Lambertian reflectance surface and fronto-parrallel view of the scene, the blurred image $y : \mathbb{R}^2 \to \mathbb{R}$ is a sharp image $x : \mathbb{R}^2 \to \mathbb{R}$ transformed by the homography matrix $\mathcal{H}(\boldsymbol{\theta}(t))$ and integrated over the exposure time interval $t \in [0, T]$::

$$y(\boldsymbol{n}) = \frac{1}{T}\int_0^T x(\mathcal{H}(\boldsymbol{\theta}(t))\boldsymbol{n})\mathrm{d}t + \epsilon(\boldsymbol{n}), \tag{5}$$

where ϵ is the measurement noise. Equivalently, the blur image model in (5) can be written in terms of the blur kernel:

$$
\begin{aligned}
y(\boldsymbol{n}) &= \frac{1}{T}\int_0^T x(\mathcal{H}(\boldsymbol{\theta}(t))\boldsymbol{n})\mathrm{d}t + \epsilon(\boldsymbol{n}) \\
&= \frac{1}{T}\int_0^T \int_{-\pi}^{\pi} x(\mathcal{H}(\boldsymbol{\psi})\boldsymbol{n})\delta(\boldsymbol{\psi} - \boldsymbol{\theta}(t))\mathrm{d}\boldsymbol{\psi}\mathrm{d}t + \epsilon(\boldsymbol{n}) \\
&= \int_{-\pi}^{\pi}\left\{\frac{1}{T}\int_0^T \delta(\boldsymbol{\psi} - \boldsymbol{\theta}(t))\mathrm{d}t\right\}x(\mathcal{H}(\boldsymbol{\psi})\boldsymbol{n})\mathrm{d}\boldsymbol{\psi} + \epsilon(\boldsymbol{n}) \\
&= \int_{-\pi}^{\pi} k_{\boldsymbol{\theta}}(\boldsymbol{\psi})x(\mathcal{H}(\boldsymbol{\psi})\boldsymbol{n})\mathrm{d}\boldsymbol{\psi} + \epsilon(\boldsymbol{n}), \tag{6}
\end{aligned}
$$

where the blur kernel

$$k_{\boldsymbol{\theta}}(\boldsymbol{\psi}) = \frac{1}{T}\int_0^T \delta(\boldsymbol{\psi} - \boldsymbol{\theta}(t))\,\mathrm{d}t \tag{7}$$

is computed as an accumulated time weight at rotation $\boldsymbol{\psi}$.

IMU is a device that measures the angular speed of a camera. Fig. 3(c) shows an example of 3-axis rotation measured by the IMU. Based on the angular speed, we can compute the trajectory of the camera's rotation [11], which we denote by $\boldsymbol{\theta}_0(t)$. If the IMU is error-free and perfectly synchronized with the camera,

then we are able to recover the blur kernel $k_{\boldsymbol{\theta}_0}(\boldsymbol{\psi})$ via (7) and perform non-blind deblurring to reconstruct a sharp image.

The IMUs in most cameras are unfortunately prone to errors stemming from noise, bias or drift, and are sensitive to gravity, which are accumulated when computing the camera rotation from its angular speed. In the mobile platforms, the delay between shutter and the IMU may dynamically change depending on the other system calls in the queue. Thus $\boldsymbol{\theta}_0(t)$ is expected to be a time-delayed, biased, and error prone measurement of the real camera motion $\boldsymbol{\theta}(t)$. As a result, the recovered blur kernel $k_{\boldsymbol{\theta}_0}(\boldsymbol{\psi})$ does not necessarily yield a satisfactory deblurring result [see Fig. 2 (b) and (e)].

B. Blind and Non-Blind Deblurring Via Energy Minimization

Blind deblurring is a process of recovering the sharp image and the blur kernel given a blurry image observation. Solving such a problem is challenging due to the fact that the system is underdetermined [See Fig. 2(f)]. On the other hand, non-blind deblurring refers to the estimation of the sharp image when the blur kernel is known. Obviously, the system for non-blind deblurring is less underdetermined compared to blind case, yielding a more reliable reconstruction in most of the cases.

A typical blind deblurring method seeks the blur kernel weights $k(\boldsymbol{\psi})$ and the sharp image x that minimizes an objective energy. Such minimization typically takes the form [1]–[3], [5]–[9]:

$$\{\hat{x}, \hat{k}\} = \underset{x,k}{\arg\min}\ \underbrace{\|y - \mathcal{P}\{x, k\}\|_2^2}_{\text{fidelity}} + \underbrace{\alpha E_1(x)}_{\text{regularization on } x} \\ + \underbrace{\beta E_2(k)}_{\text{regularization on } k}, \tag{8}$$

where

$$\mathcal{P}\{x, k\}(\boldsymbol{n}) = \int_{-\pi}^{\pi} k(\boldsymbol{\psi})x(\mathcal{H}(\boldsymbol{\psi})\boldsymbol{n})\mathrm{d}\boldsymbol{\psi}. \tag{9}$$

The blind deblurring in (8) is carried out by iteratively solving:

$$\hat{x} = \underset{x}{\arg\min}\ \|y - \mathcal{P}\{x, k\}\|_2^2 + \alpha E_1(x), \tag{10}$$

$$\hat{k} = \underset{k}{\arg\min}\ \|y - \mathcal{P}\{x, k\}\|_2^2 + \beta E_2(k). \tag{11}$$

Known as fixed-point iteration, (10) is solved by fixing k; (11) is solved by fixing x; and (10) and (11) are repeated until they have converged. In the non-blind case, $\hat{x}$ is estimated by using (10) only [19], [22]. Indeed, in the case of IMU-based image deblurring, the blur kernel $k_{\boldsymbol{\theta}_0}(\boldsymbol{\psi})$ is computed based on IMU measurements $\boldsymbol{\theta}_0$ using (7). This is used in conjunction with (10) to recover the sharp image $\hat{x}$.

A desired $E_1(x)$ is expected to promote image sparsity in a transform domain (e.g. image derivative). For example, Cho *et al.* uses simple L_2 norm regularization of the gradient image, but with additional shock filtering and bilateral filtering to suppress small image details; Shan *et al.* [3] uses a concatenation of two piece-wise continuous functions to model the sparsity of the image gradient density; Cai *et al.* proposed L_1 norm regularization of image in the framelet domain [23]; Zoran and Weiss [24] takes advantage of the learned latent sharp image features; Xu *et al.* [6] proposed an image prior term that is an approximation to L_0 norm of the image gradients taking the following form:

$$E_1(x) = \sum_{o \in \{h,v\}} \sum_{\boldsymbol{n}} \phi(\partial_o x(\boldsymbol{n})), \qquad (12)$$

where $\phi(\cdot)$ is an approximation to the L_0 norm:

$$\phi(\partial_o x(\boldsymbol{n})) = \begin{cases} \frac{1}{\epsilon^2} |\partial_o x(\boldsymbol{n})|^2, & \text{if } |\partial_o x(\boldsymbol{n})| \leq \epsilon \\ 1, & \text{else} \end{cases}, \qquad (13)$$

where ϵ is a parameter controls the image detail scale (see [6]). The operators ∂_h, ∂_v are the horizontal and vertical derivatives, respectively. Krishnan *et al.* [18] normalized the L_1 norm of the image gradients by its L_2 norm:

$$E_1(x) = \sum_{o \in \{h,v\}} \frac{\|\partial_o x\|_1}{\|\partial_o x\|_2}. \qquad (14)$$

The blur kernel prior $E_2(k)$ typically takes the form $E_2(k) = \|k\|_1$ ([3], [18]) or $E_2(k) = \|k\|_2^2$ ([5], [6], [25], [26]), based on the intuition that blur kernel itself is sparse.

Under the special case where the blur kernel is spatially uniform, (9) simplifies to a convolution:

$$\mathcal{P}'\{x, k\} = x \star k, \qquad (15)$$

where $\star$ denotes the convolution operator [1], [3], [5]–[8]. Methods that make such simplification are considerably more stable due to reduced parameters that are unknown.

The major disadvantage of (8) is that IMU is not utilized, even though such sensor is already widely available in today's consumer imaging devices. As we prove in the next section, IMU measurements help to overcome the ill-posedness of the blind deblurring techniques by constraining the set of feasible solutions.

III. Image-IMU Complementary Deblurring

The bias in a blur estimation reconstructed from the IMU measurements stems from a number of sources, including the accumulation of the gyroscope and accelerometer error over time, an unknown delay between the camera exposure and the IMU starting time, the IMU random walk noise, an inaccurate

calibration of the camera intrinsic parameters, and the invalidity of the constant gravity assumption. Due to the fact that even small errors in the blur estimation cause deblurring artifacts, a IMU-based blur kernel estimation is not accurate enough for the non-blind deblurring in (10) (Fig. 2(b)). Thus, further refinement of IMU measurements using an energy minimization is desired. In this paper, we focus on the 3-DOF gyroscope measurements—it is justifiable when the scene distance is sufficiently far or when the blur caused by the acceleration is negligible [9]. Our goal is to combine the blur information from the image sensor data and the IMU measurements to yield better blur and image reconstructions.

A. Optimization Over IMU Measurement

We propose to recover the sharp image x and the corrected IMU rotation by:

$$\left\{\hat{x}, \hat{\boldsymbol{\theta}}\right\} = \arg\min_{x, \boldsymbol{\theta}} \underbrace{\|\boldsymbol{y} - \mathcal{Q}\{x, \boldsymbol{\theta}\}\|_2^2}_{\text{image fidelity}} + \underbrace{\lambda \|\boldsymbol{\theta} - \boldsymbol{\theta}_0\|_p}_{\text{IMU fidelity}}$$
$$+ \underbrace{\alpha E_1(x)}_{\text{regularization on } x}, \qquad (16)$$

where $E_1(x)$ is the same regularization term as the one in (8), and

$$\mathcal{Q}\{x(\boldsymbol{n}), \boldsymbol{\theta}\} = \frac{1}{T} \int_0^T x(\mathcal{H}(\boldsymbol{\theta}(t))\boldsymbol{n}) \mathrm{d}t. \qquad (17)$$

Comparing to (8), our proposed energy function in (16) replaces the regularization term $E_2(\cdot)$ by the IMU fidelity term $\|\boldsymbol{\theta} - \boldsymbol{\theta}_0\|_p = \int_0^T \|\boldsymbol{\theta}(t) - \boldsymbol{\theta}_0(t)\|_p \mathrm{d}t$, and modifies the image fidelity term as $\|\boldsymbol{y} - \mathcal{Q}\{x, \boldsymbol{\theta}\}\|_2^2$ to ensure that our estimates $\left\{\hat{x}, \hat{\boldsymbol{\theta}}\right\}$ are consistent with observations $\{y, \boldsymbol{\theta}_0\}$. However, the cost function (16) is not convex, owing to the fact that $x(\mathcal{H}(\boldsymbol{\theta}(t))\boldsymbol{n})$ is a nonlinear function of $\boldsymbol{\theta}$.

Before proceeding further, consider an obvious alternative to (16) taking the form:

$$\left\{\hat{x}, \hat{k}\right\} = \arg\min_{x, k} \|y - \mathcal{P}\{x, k\}\|_2^2 + \underbrace{\lambda \|k - k_{\boldsymbol{\theta}_0}\|_q}_{\text{IMU fidelity}}$$
$$+ \alpha E_1(x). \qquad (18)$$

Here, (18) is a modification on (8) by introducing a different IMU fidelity term $\|k - k_{\boldsymbol{\theta}_0}\|_q = \int_{-\pi}^{\pi} \|k(\boldsymbol{\psi}) - k_{\boldsymbol{\theta}_0}(\boldsymbol{\psi})\|_q \mathrm{d}\boldsymbol{\psi}$, where $k_{\boldsymbol{\theta}_0}$ is the blur kernel inferred from IMU measured $\boldsymbol{\theta}_0$ using (7). The advantage of (18) over the (16) is that the cost function in (18) is convex when q is 1 or 2, and the minimizer of (18) can be found by the solvers that already solve (8).

The major disadvantage to (18), however, is that the IMU fidelity cost function $\|k_{\boldsymbol{\theta}} - k_{\boldsymbol{\theta}_0}\|_q$ is not useful. Consider Fig. 4(a)–(c), where we compare $\boldsymbol{\theta}(t)$ (green plot) and $\boldsymbol{\theta}'(t)$ (red plot) to the IMU measurement $\boldsymbol{\theta}_0(t)$ (blue plot). Due to the fact that $\boldsymbol{\theta}'(t)$ is clearly more similar to $\boldsymbol{\theta}_0(t)$, the blur kernel $k_{\boldsymbol{\theta}'}(\boldsymbol{\psi})$ (red plot) in Fig. 4(d) is more similar to $k_{\boldsymbol{\theta}_0}(\boldsymbol{\psi})$ (blue plot) than $k_{\boldsymbol{\theta}}(\boldsymbol{\psi})$ (green plot) is to $k_{\boldsymbol{\theta}_0}(\boldsymbol{\psi})$. Yet, the IMU fidelity costs of the form $\|k_{\boldsymbol{\theta}} - k_{\boldsymbol{\theta}_0}\|_2$ and $\|k_{\boldsymbol{\theta}'} - k_{\boldsymbol{\theta}_0}\|_2$ are equal, owing to the fact $\|k - k_{\boldsymbol{\theta}_0}\|_q$ penalizes heavily when the supports of k and
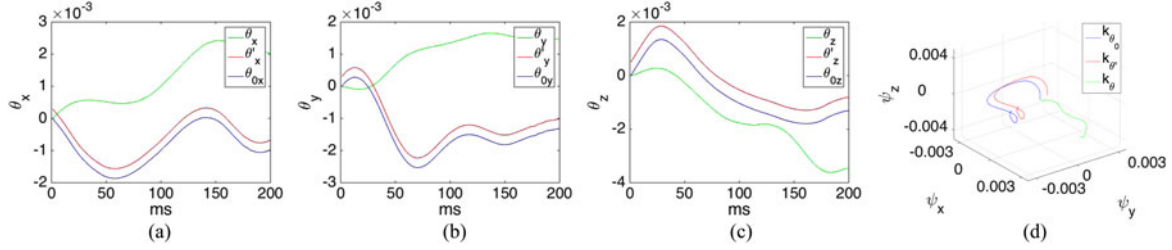
Fig. 4. Energy minimization in (16) reflects the behavior of the IMU fidelity term we seek better than (18). Let $\boldsymbol{\theta}_0(t) = (\theta_{0x}(t), \theta_{0y}(t), \theta_{0z}(t))$ (blue plot) be an actual IMU measurement. Computed based on (18), the functions $\boldsymbol{\theta}(t) = (\theta_x(t), \theta_y(t), \theta_z(t))$ (green plot) and $\boldsymbol{\theta}'(t) = (\theta'_x(t), \theta'_y(t), \theta'_z(t))$ (red plot) yield the same IMU fidelity costs ($\|\|k_{\boldsymbol{\theta}} - k_{\boldsymbol{\theta}_0}\|_2 = \|\|k_{\boldsymbol{\theta}'} - k_{\boldsymbol{\theta}_0}\|_2 = 1.18 \times 10^{-2}$), even though $\boldsymbol{\theta}'(t)$ is clearly more similar to $\boldsymbol{\theta}_0(t)$ than $\boldsymbol{\theta}(t)$. By contrast, IMU fidelity costs in (16) favors $\boldsymbol{\theta}'(t)$ over $\boldsymbol{\theta}(t)$ ($\|\|\boldsymbol{\theta} - \boldsymbol{\theta}_0\|_2 = 2.8 \times 10^{-3}$ and $\|\|\boldsymbol{\theta}' - \boldsymbol{\theta}_0\|_2 = 8.6 \times 10^{-5}$).

$k_{\boldsymbol{\theta}_0}$ do not overlap significantly. Indeed, we have implemented (18), but it did not yield a convincing improvement over (8).

By contrast, the fidelity costs $\|\boldsymbol{\theta} - \boldsymbol{\theta}_0\|_2$ and $\|\boldsymbol{\theta}' - \boldsymbol{\theta}_0\|_2$ computed from Fig. 4(a)–(c) are 2.8×10^{-3} and 8.6×10^{-5}, respectively. This clearly reflects the behavior of an IMU fidelity term that we seek. Hence, despite the lack of convexity, we conclude that deblurring by energy minimization in (16) is superior to the deblurring by (18). In the following section, we introduce a novel convex approximation to (16).

B. Convex Approximation by a Distance Transform

Consider an L_p distance transform of the form

$$\mathcal{D}_p(\boldsymbol{\psi}, \boldsymbol{\theta}_0) = \min_{t' \in [0,T]} \|\boldsymbol{\psi} - \boldsymbol{\theta}_0(t')\|_p. \quad (19)$$

In order to minimize the non-convex energy function in (16), we consider an approximation

$$\|\boldsymbol{\theta}(t) - \boldsymbol{\theta}_0(t)\|_p \approx \mathcal{D}_p(\boldsymbol{\theta}(t), \boldsymbol{\theta}_0)$$
$$= \min_{t' \in [0,T]} \|\boldsymbol{\theta}(t) - \boldsymbol{\theta}_0(t')\|_p. \quad (20)$$

That is, the L_p error between $\boldsymbol{\theta}(t)$ and $\boldsymbol{\theta}_0(t')$ is minimal when $t \approx t'$. This intuition gives rise to the following approximation:

Theorem 1 (IMU Linearization and Convex Relaxation):

$$\|\boldsymbol{\theta} - \boldsymbol{\theta}_0\|_p \approx T\|\mathcal{D}_p(\boldsymbol{\psi}, \boldsymbol{\theta}_0)k_{\boldsymbol{\theta}}(\boldsymbol{\psi})\|_1, \quad (21)$$

where $k_{\boldsymbol{\theta}}(\boldsymbol{\psi}) = \frac{1}{T}\int_0^T \delta(\boldsymbol{\psi} - \boldsymbol{\theta}(t)) \mathrm{d}t$
and $\|\mathcal{D}_p(\boldsymbol{\psi}, \boldsymbol{\theta}_0)k_{\boldsymbol{\theta}}(\boldsymbol{\psi})\|_1 = \int_{-\pi}^{\pi} \mathcal{D}_p(\boldsymbol{\psi}, \boldsymbol{\theta}_0)k_{\boldsymbol{\theta}}(\boldsymbol{\psi})\mathrm{d}\boldsymbol{\psi}$.
Proof:

$$\|\boldsymbol{\theta} - \boldsymbol{\theta}_0\|_p = \int_0^T \|\boldsymbol{\theta}(t) - \boldsymbol{\theta}_0(t)\|_p \mathrm{d}t$$

$$\approx \int_0^T \mathcal{D}_p(\boldsymbol{\theta}(t), \boldsymbol{\theta}_0) \mathrm{d}t$$

$$= \int_0^T \int_{-\pi}^{\pi} \mathcal{D}_p(\boldsymbol{\psi}, \boldsymbol{\theta}_0)\delta(\boldsymbol{\psi} - \boldsymbol{\theta}(t))\mathrm{d}\boldsymbol{\psi}\mathrm{d}t$$

$$= \int_{-\pi}^{\pi} \mathcal{D}_p(\boldsymbol{\psi}, \boldsymbol{\theta}_0)\int_0^T \delta(\boldsymbol{\psi} - \boldsymbol{\theta}(t))\mathrm{d}t\mathrm{d}\boldsymbol{\psi}$$

$$= T\int_{-\pi}^{\pi} \mathcal{D}_p(\boldsymbol{\psi}, \boldsymbol{\theta}_0)k_{\boldsymbol{\theta}}(\boldsymbol{\psi})\mathrm{d}\boldsymbol{\psi}. \quad (22)$$

$\square$
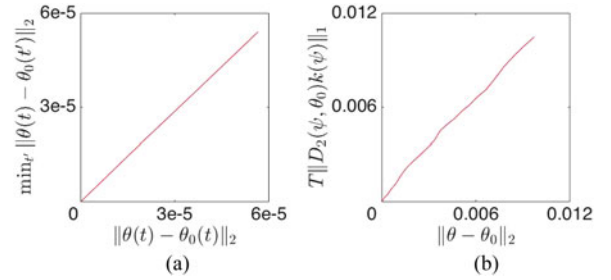
Fig. 5. Comparison of the approximations accuracy in (20) and (21). (a) $\min_{t' \in [0,T]} \|\boldsymbol{\theta}(t) - \boldsymbol{\theta}_0(t')\|_2^2$ and $\|\boldsymbol{\theta}(t) - \boldsymbol{\theta}_0(t)\|_2^2$ by adding different levels of drift. (b) Comparison of $\|\boldsymbol{\theta} - \boldsymbol{\theta}_0\|_2^2$ and $T\|\mathcal{D}_2(\boldsymbol{\psi}, \boldsymbol{\theta}_0)k_{\boldsymbol{\theta}}(\boldsymbol{\psi})\|_1$ in Theorem 1 by adding different levels of drift. A $45°$ line indicates that the approximation in (20) holds.

Fig. 5 verifies that our approximations are accurate. Fig. 5(a) compares $\|\boldsymbol{\theta}(t) - \boldsymbol{\theta}_0(t)\|_2$ to $\mathcal{D}_2(\boldsymbol{\theta}(t), \boldsymbol{\theta}_0(t))$, where $\boldsymbol{\theta}_0(t)$ is as shown in Fig. 3(c), and $\boldsymbol{\theta}(t)$ is $\boldsymbol{\theta}_0(t)$ corrupted by random drifts. Fig. 5(b) compares $\|\boldsymbol{\theta} - \boldsymbol{\theta}_0\|_2$ to $T\|\mathcal{D}_2(\boldsymbol{\psi}, \boldsymbol{\theta}_0)k_{\boldsymbol{\theta}}(\boldsymbol{\psi})\|_1$ in a similar manner. In both cases, the approximations of (20) and (21) are justified.

Fig. 6 shows examples of distance transform $\mathcal{D}_2(\boldsymbol{\psi}, \boldsymbol{\theta}_0)$. The blur kernel in Fig. 6(a) is mapped to a distance transform in Fig. 6(b). A two dimensional blur kernel (for uniform blur kernel case) in the form of PSF as shown in Fig. 6(c) also has a two dimensional distance transform in Fig. 6(d).

Theorem 1 is significant because we replaced IMU fidelity term by a weighted L_1 norm of $k_{\boldsymbol{\theta}}$. Substituting (21) into (16), we have

$$\{\hat{x}, \hat{\boldsymbol{\theta}}\} \approx \arg\min_{x, \boldsymbol{\theta}} \|y - \mathcal{P}(x, k_{\boldsymbol{\theta}})\|_2^2 + \lambda T\|\mathcal{D}_p(\boldsymbol{\psi}, \boldsymbol{\theta}_0)k_{\boldsymbol{\theta}}(\boldsymbol{\psi})\|_1$$
$$+ \alpha E_1(x). \quad (23)$$

Notice that (23) is now entirely written in terms of $k_{\boldsymbol{\theta}}(\boldsymbol{\psi})$. Hence the sharp image $\hat{x}$ and blur kernel $k_{\hat{\boldsymbol{\theta}}}$ reconstructed from (23) are same as

$$\{\hat{x}, \hat{k}\} = \arg\min_{x, k} \|y - \mathcal{P}(x, k)\|_2^2 + \lambda T\|\mathcal{D}_p(\boldsymbol{\psi}, \boldsymbol{\theta}_0)k(\boldsymbol{\psi})\|_1$$
$$+ \alpha E_1(x). \quad (24)$$

The advantage to this technique is that $\mathcal{D}_p(\boldsymbol{\psi}, \boldsymbol{\theta}_0)$ is a pre-computed weight, independent of $\boldsymbol{\theta}$ or k. Thus (24) is convex,
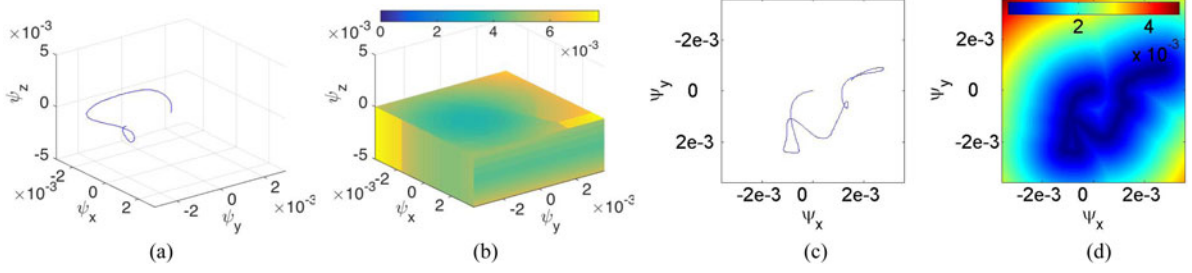
Fig. 6.   Illustration of distance transform $\mathcal{D}_2(\boldsymbol{\psi}, \boldsymbol{\theta}_0)$. (a) blur kernel, (b) distance transform $\mathcal{D}_2(\boldsymbol{\psi}, \boldsymbol{\theta}_0)$ of (a), (c) blur kernel when $\theta_z = 0$, and (d) distance transform $\mathcal{D}_2(\boldsymbol{\psi}, \boldsymbol{\theta}_0)$ of (c).
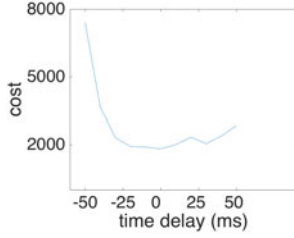
Fig. 7.   Cost function (23) is insensitive to synchronization issues. We manually added time delays to $\boldsymbol{\theta}_0$ from -50 ms to 50 ms with an 10 ms increment. The blur kernel estimation performance is typically stable within ± 30 ms range.

where its minimizer can be found by the solvers that already solve (8).

After (24) is minimized, one can do better if the final deblurring is performed using a high quality non-blind deblurring method, such as the method in [19]. This is a common practice among the blind deblurring techniques [6], [7], [18], [27] and we follow this practice here as well.

C. Image-IMU Synchronization

One key benefit to the approximations in (23) is that it is insensitive to the synchronization issues. To understand why this is the case, recall (19). The distance transform is largely invariant to the synchronization in the following sense:

$$\min_{t' \in [0,T]} \|\boldsymbol{\psi} - \boldsymbol{\theta}_0(t')\|_p = \min_{t' \in [0,T]} \|\boldsymbol{\psi} - \boldsymbol{\theta}_0(t' + \Delta_t)\|_p \quad (25)$$

for some time shift Δ_t if

$$\min_{t' \in [\Delta_t, T]} \|\boldsymbol{\psi} - \boldsymbol{\theta}_0(t')\|_p \le \min_{t' \in [0, \Delta_t] \cup [T, T + \Delta_t]} \|\boldsymbol{\psi} - \boldsymbol{\theta}_0(t')\|_p. \quad (26)$$

Thanks to (25), the IMU linearization in (21) tolerates time delays causing synchronization errors to a degree. We experimentally verified our claim in Fig. 7. The cost function in (23) was computed by introducing synchronization errors in the range $\Delta_t \in [-50 \text{ ms}, 50 \text{ ms}]$ to an actual IMU measurement $\boldsymbol{\theta}_0$. The cost (23) remained stable within $\Delta_t \in [-30 \text{ ms}, 30 \text{ ms}]$ range.

IV. EXPERIMENT

A. Setup

1) Hardware Systems: We evaluate our proposed method using the real camera data. Prototype system shown in Fig. 3(b) includes Nikon D90 camera, Raspberry Pi as controller, and InvenSense MPU 9250 IMU sensor. IMU data log module is implemented using C++ and the sampling frequency is 1000 Hz. Blind deblurring is implemented by MATLAB and executed on PC using Intel(R) Core(TM) i7-2600 CPU @ 3.4G Hz with 16 GB memory. Processing 800×800 uniform blur color image using (24) typically takes 4 and 12 seconds with the image priors in [6] and [18], respectively.

The real data experiment is conducted on a raw sensor data captured by Nikon D90 with shutter speeds in the range of $1/20 - 1/2$ second, and 18 mm focal length. The raw data was first treated with demosaicking method of [28]; then the pixel neighborhood of 2×2 was averaged and the image was downsampled by 2 to ensure that the demosaicking artifacts has minimal impact on the deblurring process. We performed a gamma correction after deblurring [29].

2) Image Prior Example and Solvers: Recall the fixed point iteration in (10) and (11). With the IMU fidelity term, we use:

$$\hat{x} = \arg\min_k \|y - \mathcal{P}(x,k)\|_2 + \alpha E_1(x), \quad (27)$$

$$\hat{k} = \arg\min_k \|y - \mathcal{P}(x,k)\|_2 + \lambda T \|\mathcal{D}_p(\boldsymbol{\psi}, \boldsymbol{\theta}_0) k(\boldsymbol{\psi})\|_1. \quad (28)$$

We adopt the image prior terms $E_1(x)$ proposed in [6] and [18]. We refer readers to [6] and [18] for detail implementation of solving (27) using the prior terms of (12) and (14).

The solution to (28) is equivalent to:

$$\hat{k} = \frac{\left\{ \arg\min_k \|y - \tilde{\mathcal{P}}(x,k)\|_2^2 + \lambda \|k\|_1 \right\} + \zeta}{\mathcal{D}_p(\boldsymbol{\psi}, \boldsymbol{\theta}_0) + \zeta}, \quad (29)$$

where we added a small constant ζ to prevent a devision by zero. Readers may notice the similarity of (29) to the classical kernel estimation form—the difference is in the denominator, which is designed to solve (28) instead of (11). The detailed calculations of $\mathcal{P}(x,k)$ and $\tilde{\mathcal{P}}(x,k)$ are shown in Appendix A. Notice that (29) is a lasso problem and can be solved efficiently by the methods in [18], [19], [30]–[34]. We use [30] for the general case and [18] for the uniform blur. All methods in Figs. 8–12
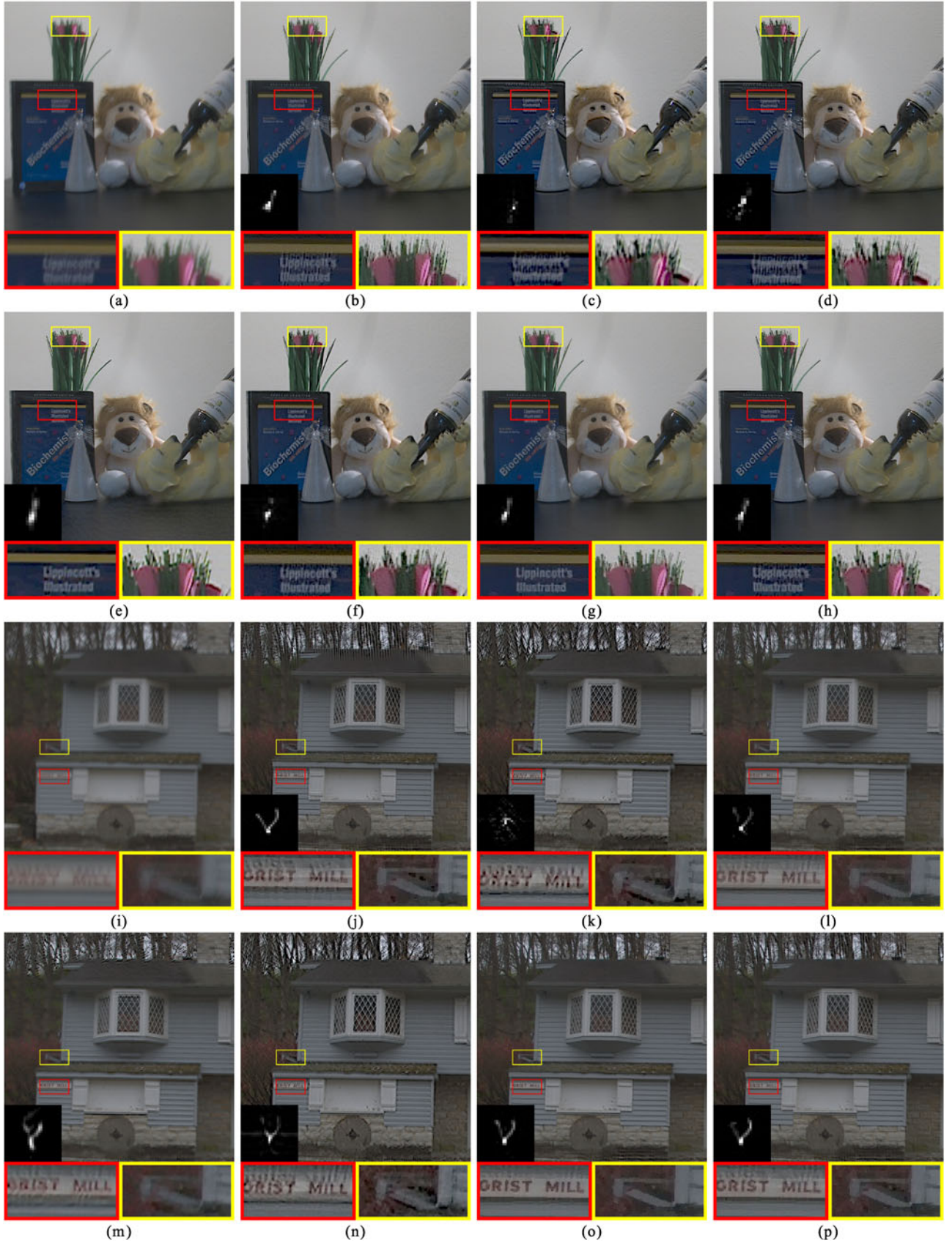
Fig. 8. Deblurring example (uniform blur). (a, i) Blurry input images. (b, j) IMU blur kernel and non-blind deblurring of [19]. (c, k) Method in [27]. (d, l) Method in [35]. (e, m) Method in [6]. (f, n) Method in [18]. (g, h, o, p) Proposed method in (24). The regularizer $E_1(x)$ used in (g, o) and (h, p) are [6] and [18], respectively.
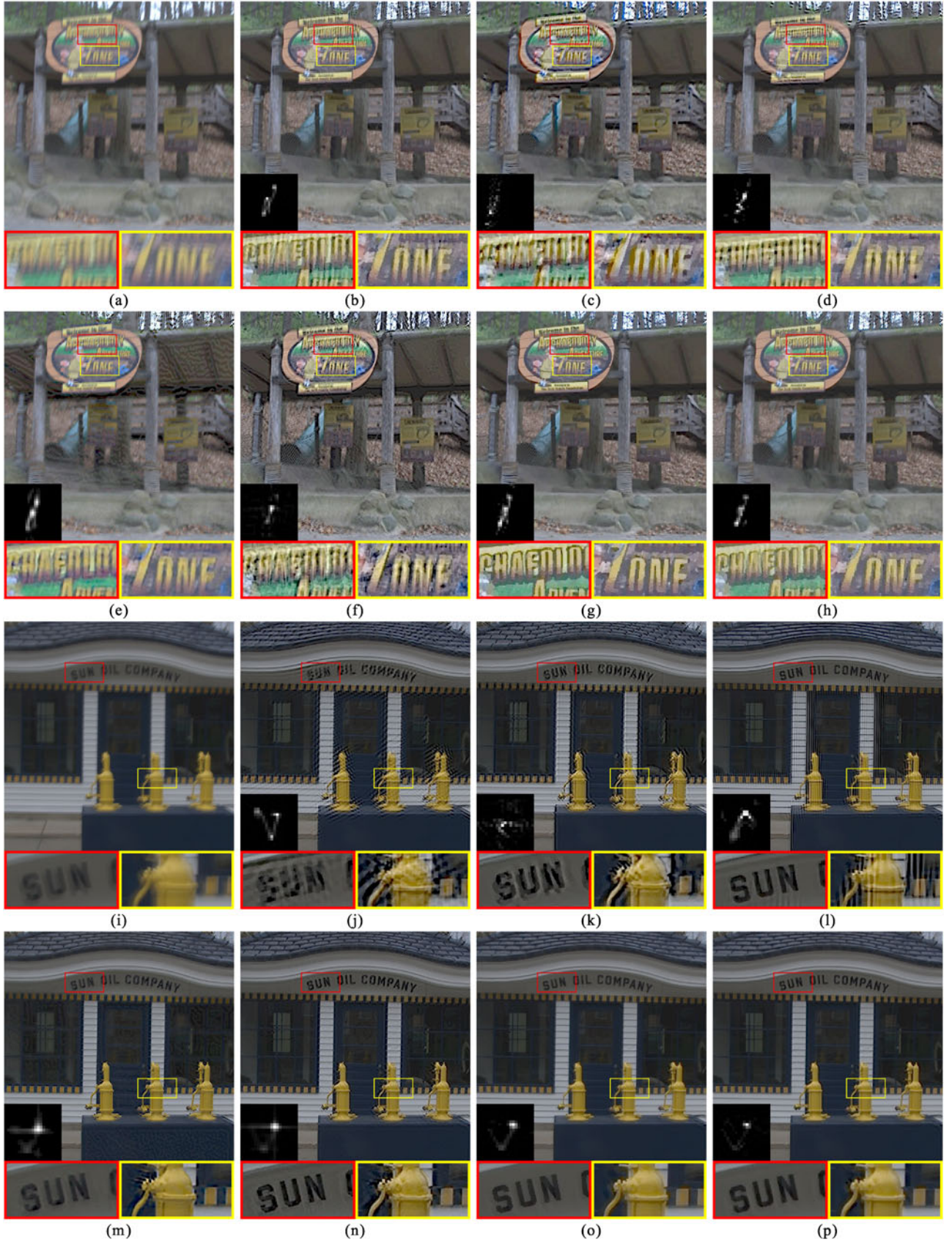
Fig. 9. Deblurring example (uniform blur). (a, i) Blurry input images. (b, j) IMU blur kernel and non-blind deblurring of [19]. (c, k) Method in [27]. (d, l) Method in [35]. (e, m) Method in [6]. (f, n) Method in [18]. (g, h, o, p) Proposed method in (24). The regularizer $E_1(x)$ used in (g, o) and (h, p) are [6] and [18], respectively.

Fig. 10. Deblurring example (uniform blur). (a, i) Blurry input images. (b, j) IMU blur kernel and non-blind deblurring of [19]. (c, k) Method in [27]. (d, l) Method in [35]. (e, m) Method in [6]. (f, n) Method in [18]. (g, h, o, p) Proposed method in (24). The regularizer $E_1(x)$ used in (g, o) and (h, p) are [6] and [18], respectively.

Fig. 11. Deblurring example (uniform blur). (a, i) Blurry input images. (b, j) IMU blur kernel and non-blind deblurring of [19]. (c, k) Method in [27]. (d, l) Method in [35]. (e, m) Method in [6]. (f, n) Method in [18]. (g, h, o, p) Proposed method in (24). The regularizer $E_1(x)$ used in (g, o) and (h, p) are [6] and [18], respectively.

Fig. 12. Deblurring example (non-uniform blur). (a, e, i) Blurry input images. (b, f, j) IMU blur kernel and non-blind deblurring of [19]. (c, g, k) Method in [9]. (d, h, l) Proposed method in (24). The regularizer $E_1(x)$ is [6].

use [19] to perform the final non-blind deblurring with $L_{1/2}$ norm regularization.

3) Parameters: We use the same image prior parameters α used in [6] and [18]. We set $\lambda = 5 \times 10^{-4}$ and $\lambda \in [5 \times 10^{-1}, 2]$ for the uniform and the non-uniform blurs, respectively. Notice that one can use a large λ if the IMU measurement is accurate or the image is noisy. In our experiment, ψ is sampled from $\psi_x \in [-0.0045\,\mathrm{rad}, 0.0045\,\mathrm{rad}]$, $\psi_y \in [-0.0045\,\mathrm{rad}, 0.0045\,\mathrm{rad}]$ and $\psi_z \in [-0.01\,\mathrm{rad}, 0.01\,\mathrm{rad}]$ with the increments of $0.0003\,\mathrm{rad}, 0.0003\,\mathrm{rad}, 0.002\,\mathrm{rad}$, respectively.

B. Uniform Blur Examples

Blur is approximately uniform in Figs. 8–11(a, i) when θ_z is small (average variance of $\theta_{0z}(t)$ in Figs. 8–11 is 5.2×10^{-7}).

The reconstructions directly using the IMU measurement (use non-blind deblurring [19] [6], [9], [14]) are generally unsatisfactory due to the IMU sensor drift and synchronization issue (Figs. 10–11(b, j)), though sometimes they are acceptable (Figs. 8–9(b, j)). On the other hand, image-based blind deblurring methods in [6], [18], [27], [35] yield satisfactory sharp image reconstructions in Figs. 8(l) and 11(e), (l), (m), (n), or partially acceptable images in Figs. 8(e) and (f), 9(e) and 10(e) and (l). Yet the performance is still not stable as evidenced in the remainder. Proposed method by comparison infers the blur kernels from both IMU measurements and image sensor data, therefore showing improved sharp image reconstructions overall in Figs. 8–11(g), (h), (o), (p). In particular, it is interesting to compare Figs. 8–11(e), (f), (m), (n) to (g), (h), (o), (p) as they use the same image regularizer $E_1(x)$.

C. Non-Uniform Blur Examples

In Figs. 12(a), (e), (i), the blur kernels are spatially vary-ing (average variance of $\theta_{0z}(t)$ is 3.3×10^{-6}). As evidenced in Figs. 12(c), (g), (k), the non-blind deblurring using the IMU measurements suffers from severe ringing artifacts. The popu-lar image-based blind deblurring techiques such as [9] are also unstable (Fig. 12(d), (h), (l)). As shown in Fig. 12(b), (f), (j), the proposed method utilizes both the image and the IMU informa-tion to yield satisfactory sharp image reconstructions.

V. CONCLUSION

We proposed a novel image deblurring method designed to minimize an energy function comprised of image fidelity, image regularization and IMU fidelity terms. We recover a sharp image consistent with the observed blurry image and IMU measure-ments. Proposed method replaced the non-convex IMU fidelity term by its convex approximation using a distance transform that can be pre-computed. Thus the energy minimization can be solved with the existing solvers. Our approach was shown theoretically and experimentally to tolerate moderate levels of synchronization errors.

The resultant deblurring is superior to the blind deblurring as well as the IMU-based non-blind deblurring. However, our deblurring results are by no means perfect. Deblurring artifacts are evidenced in the zoomed portions of the deblurred images, though much less in severity than the existing techniques. Our technique will also fail in presence of any specular highlights (which violate the Lambertian assumption in (5)) or when the objects in the scene are close to the camera (which violates the assumptions made in Section II.A). Nevertheless, the proposed combination of IMU data and blind image deblurring improves on the state-of-the-art deblurring techniques.

APPENDIX A
DISCRETE QUANTIZATION

Let $\ell \in [1, \mathcal{L}]$ denote the quantized and truncated version of $\psi \in [\psi_{\min}, \psi_{\max}]$ (such that $-\pi \le \psi_{\min} \le \psi_{\max} \le \pi$). Then:

$$\mathcal{P}(x, k) = \mathcal{U}x \qquad (30)$$

or

$$\mathcal{P}(x, k) = \mathcal{V}k \qquad (31)$$

where

$$\mathcal{U}(j, m) = \sum_{\ell} \mathcal{B}(j, m, \ell)k(\ell), \quad \mathcal{U} \in \mathbb{R}^{N \times N}$$

$$\mathcal{V}(j, \ell) = \sum_{m} \mathcal{B}(j, m, \ell)x(m), \quad \mathcal{V} \in \mathbb{R}^{N \times \mathcal{L}} \qquad (32)$$

where sparse blur matrix $\mathcal{B}(\cdot, \cdot, \ell) \in \mathbb{R}^{N \times N}$ denotes a linear operation that applies homography $\mathcal{H}(\psi)$ to sharp image x. We show example of using bilinear interpolation in the Appendix B.

In fixed point iteration, $\mathcal{U}$ and $\mathcal{V}$ are used to solve x and k sub-problems, respectively. In particular, $\tilde{\mathcal{P}}(x, k)$ in (29) can be obtained by:

$$\tilde{\mathcal{P}}(x, k) = \tilde{\mathcal{V}}k, \qquad (33)$$

where

$$\tilde{\mathcal{V}}(j, \ell) = \sum_{m} \frac{\mathcal{B}(j, m, \ell)x(m)}{\mathcal{D}_p(\ell, \boldsymbol{\theta}_0)}. \qquad (34)$$

APPENDIX B
BILINEAR INTERPOLATION OF BLUR MATRIX

Let $\boldsymbol{n} = [n_h, n_v]$ denotes the two dimensional image pixel location. Let $\Lambda(\cdot) : \mathbb{Z} \to \mathbb{Z}^2$ denote index mapping function, define the bilinear operator $\mathcal{G}(\cdot, \cdot)$ interpolates a translated pixel location $\mathcal{H}(\psi)\Lambda(j) = \boldsymbol{\xi}(\ell, j) = [\xi_h, \xi_v]$:

$$\mathcal{G}(\boldsymbol{n}, \boldsymbol{\xi}) =$$
$$\delta(n_h - \lfloor \xi_h \rfloor)\delta(n_v - \lfloor \xi_v \rfloor)\{1 - (\xi_h - \lfloor \xi_h \rfloor)\}$$
$$\{1 - (\xi_v - \lfloor \xi_v \rfloor)\}$$
$$+ \delta(n_h - \lceil \xi_h \rceil)\delta(n_v - \lfloor \xi_v \rfloor)(\xi_h - \lfloor \xi_h \rfloor)\{1 - (\xi_v - \lfloor \xi_v \rfloor)\}$$
$$+ \delta(n_h - \lfloor \xi_h \rfloor)\delta(n_v - \lceil \xi_v \rceil)\{1 - (\xi_h - \lfloor \xi_h \rfloor)\}(\xi_v - \lfloor \xi_v \rfloor)$$
$$+ \delta(n_h - \lceil \xi_h \rceil)\delta(n_v - \lceil \xi_v \rceil)(\xi_h - \lfloor \xi_h \rfloor)(\xi_v - \lfloor \xi_v \rfloor), \quad (35)$$

where $\lfloor \cdot \rfloor$ is a operator takes the biggest integer not greater than its input. The sparse matrix $\mathcal{B}$ is given by following:

$$\mathcal{B}(j, m, \ell) = \mathcal{G}(\Lambda(m), \boldsymbol{\xi}(\ell, j)), \qquad (36)$$

where $\lceil \cdot \rceil$ denotes the smallest integer not less than its input.

REFERENCES

[1] J. Cai, H. Ji, and Z. Shen, "Blind motion deblurring from a single image using sparse approximation," *Comput. Vision Pattern Recog.*, vol. 62, pp. 291–294, Jan. 2009.
[2] S. Nayar and M. Ben-Ezra, "Motion-based motion deblurring," *IEEE Trans. Pattern Anal. Mach. Intell.*, vol. 26, no. 6, pp. 689–698, Jun. 2004.
[3] Q. Shan, J. Jia, and A. Agarwala, "High-quality motion deblurring from a single image," *ACM Trans. Graph.*, vol. 27, 2008, Art. no. 73.
[4] T. Cho, S. Paris, B. Horn, and W. Freeman, "Blur kernel estimation using the radon transform," in *Proc. IEEE Conf. Comput. Vision Pattern Recog.*, 2011, pp. 241–248.
[5] S. Cho and S. Lee, "Fast motion deblurring," *ACM Trans. Graphics*, vol. 28, no. 5, 2009, Art. no. 145.
[6] L. Xu, S. Zheng, and J. Jia, "Unnatural l0 sparse representation for natural image deblurring," in *Proc. IEEE Conf. Comput. Vision Pattern Recog.*, 2013, pp. 1107–1114.
[7] L. Z. S. Cho, D. Metaxas, S. Paris, and J. Wang, "Handling noise in single image deblurring using directional filters," in *Proc. IEEE Conf. Comput. Vision Pattern Recog.*, 2013, pp. 612–619.
[8] D. Perrone and P. Favaro, "Total variation blind deconvolution: The devil is in the details," in *Proc. IEEE Conf. Comput. Vision Pattern Recog.*, 2014, pp. 2909–2916.
[9] O. Whyte, J. Sivic, A. Zisserman, and J. Ponce, "Non-uniform deblurring for shaken images," in *Proc. IEEE Conf. Comput. Vision Pattern Recog.*, 2010, pp. 491–498.
[10] K. Group., (2016) Streaminput. [Online]. Available: https://www.khronos. org/streaminput/
[11] K. J. Barnard, C. E. White, and A. E. Absi, "Two-dimensional restoration of motion-degraded intensified CCD imagery," *Appl. Opt.*, vol. 38, no. 10, pp. 1942–1952, 1999.
[12] N. Joshi, S. B. Kang, C. L. Zitnick, and R. Szeliski, "Image deblurring using inertial measurement sensors," *ACM Trans. Graphics*, vol. 29, no. 4, 2010, Art. no. 30.

[13] H. Bae, C. C. Fowlkes, and P. H. Chou, "Accurate motion deblurring using camera motion tracking and scene depth," in *Proc. IEEE Workshop Appl. Comput. Vision*, 2013, pp. 148–153.

[14] O. Šindelář and F. Šroubek, "Image deblurring in smartphone devices using built-in inertial measurement sensors," *J. Electron. Imag.*, vol. 22, no. 1, 2013, Art. no. 011003.

[15] E. Ringaby and P.-E. Forssén, "A virtual tripod for hand-held video stacking on smartphones," in *Proc. IEEE Int. Conf. Comput. Photography*, 2014, pp. 1–9.

[16] S. Park and M. Levoy, "Gyro-based multi-image deconvolution for removing handshake blur," in *Proc. IEEE Conf. Comput. Vision Pattern Recog.*, 2014, pp. 3366–3373.

[17] C. Jia and B. L. Evans, "Online calibration and synchronization of cellphone camera and gyroscope," in *Proc. IEEE Global Conf. Signal Inform. Process.*, 2013, pp. 731–734.

[18] D. Krishnan, T. Tay, and R. Fergus, "Blind deconvolution using a normalized sparsity measure," in *Proc. IEEE Conf. Comput. Vision Pattern Recog.*, 2011, pp. 233–240.

[19] D. Krishnan and R. Fergus, "Fast image deconvolution using hyper-Laplacian priors," in *Proc. Adv. Neural Inform. Process. Syst.*, 2009, pp. 1033–1041.

[20] J.-Y. Bouguet, "Camera calibration toolbox for matlab," 2004.

[21] R. Hartley and A. Zisserman, *Multiple View Geometry in Computer Vision*. Cambridge, U.K.: Cambridge Univ. Press, 2003.

[22] S. Chan, R. Khoshabeh, K. Gibson, P. Gill, and T. Nguyen, "An augmented Lagrangian method for total variation video restoration," *IEEE Trans. Image Process.*, vol. 20, no. 11, pp. 3097–3111, Nov. 2011.

[23] J.-F. Cai, H. Ji, C. Liu, and Z. Shen, "Framelet-based blind motion deblurring from a single image," *IEEE Trans. Image Process.*, vol. 21, no. 2, pp. 562–572, Feb. 2012.

[24] D. Zoran and Y. Weiss, "From learning models of natural image patches to whole image restoration," in *Proc. IEEE Int. Conf. Comput. Vision*, 2011, pp. 479–486.

[25] T. Michaeli and M. Irani, "Blind deblurring using internal patch recurrence," in *Proc. Eur. Conf. Comput. Vision*, 2014, pp. 783–798.

[26] L. Yuan, J. Sun, L. Quan, and H.-Y. Shum, "Image deblurring with blurred/noisy image pairs," in *ACM Trans. Graphics*, vol. 26, no. 3, 2007, Art. no. 1.

[27] A. Levin, Y. Weiss, F. Durand, and W. T. Freeman, "Efficient marginal likelihood optimization in blind deconvolution," in *Proc. IEEE Conf. Comput. Vision Pattern Recog.*, 2011, pp. 2657–2664.

[28] E. Dubois, "Frequency-domain methods for demosaicking of Bayer-sampled color images," *IEEE Signal Process. Lett.*, vol. 12, no. 12, pp. 847–850, Dec. 2005.

[29] S. Kim, Y.-W. Tai, S. J. Kim, M. S. Brown, and Y. Matsushita, "Nonlinear camera response functions and image deblurring," in *Proc. IEEE Conf. Comput. Vision Pattern Recog.*, 2012, pp. 25–32.

[30] B. Efron, T. Hastie, I. Johnstone, R. Tibshirani *et al.*, "Least angle regression," *Ann. Statist.*, vol. 32, no. 2, pp. 407–499, 2004.

[31] S.-J. Kim, K. Koh, M. Lustig, S. Boyd, and D. Gorinevsky, "An interior-point method for large-scale l_1-regularized least squares," *IEEE J. Select. Topics Signal Process.*, vol. 1, no. 4, pp. 606–617, Dec. 2007.

[32] W. Yin, S. Osher, D. Goldfarb, and J. Darbon, "Bregman iterative algorithms for l_1-minimization with applications to compressed sensing," *SIAM J. Imag. Sci.*, vol. 1, no. 1, pp. 143–168, 2008.

[33] J. Darbon and S. Osher, "Fast discrete optimization for sparse approximations and deconvolutions," preprint, 2007.

[34] I. Daubechies, M. Defrise, and C. De Mol, "An iterative thresholding algorithm for linear inverse problems with a sparsity constraint," arXiv preprint math/0307152, 2003.

[35] A. Goldstein and R. Fattal, "Blur-kernel estimation from spectral irregularities," in *Proc. Eur. Conf. Comput. Vision*, 2012, pp. 622–635.
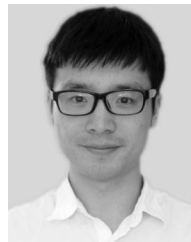
Yi Zhang (S'12–M'16) received the B.E. degree in electronic and information engineering from Nanjing University of Information Science and Technology, Nanjing, Jiangsu, China, in 2008 and the M.S. and Ph.D. degrees in electrical and computer engineering from the University of Dayton, Dayton, OH, USA, in 2011 and 2015, respectively. He is currently a Research Scientist at Ford Research and Innovation Center, Palo Alto, CA, USA. His current research interests include image processing, statistical signal processing, computer vision, and deep learning.
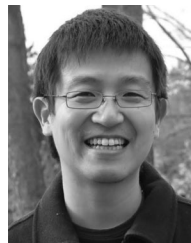
Keigo Hirakawa (S'00–M'05–SM'11) received the B.S. (Hons.) degree in electrical engineering from Princeton University, Princeton, NJ, USA, in 2000, the M.S. and Ph.D. degrees in electrical and computer engineering from Cornell University, Ithaca, NY, USA, in 2003 and 2005, respectively, and the M.M. degree (Hons.) in Jazz Performance Studies from the New England Conservatory of Music, Boston, MA, USA, in 2006. From 2006 to 2009, he was a Research Associate at Harvard University, Cambridge, MA. He is currently an Associate Professor at the University of Dayton, Dayton, OH, USA. He heads the Intelligent Signal Systems Laboratory, University of Dayton, where the group focuses on statistical signal processing, color image processing, and computer vision.